Extrinsic and intrinsic contributions to the electrostrain in precipitation-hardened barium calcium titanate

Changhao Zhao, Mao-Hua Zhang, Jürgen Rödel, et al.
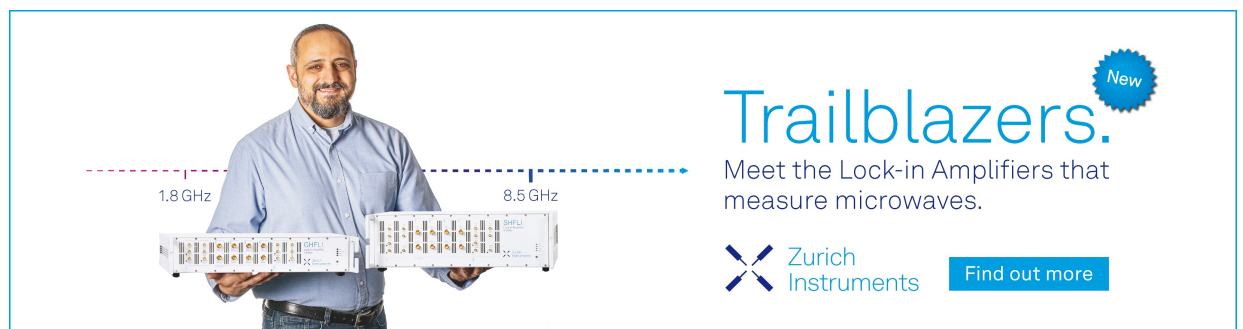
View Online   Export Citation   CrossMark

AIP Publishing

Extrinsic and intrinsic contributions to the electrostrain in precipitation-hardened barium calcium titanate

View Online   Export Citation   CrossMark

Changhao Zhao,[1,a)] (iD) Mao-Hua Zhang,[1] (iD) Jürgen Rödel,[1] (iD) and Jurij Koruza[2,a)] (iD)

AFFILIATIONS

[1]Department of Materials and Earth Sciences, Nonmetallic Inorganic Materials, Technical University of Darmstadt, Alarich-Weiss-
 Straße 2, 64287 Darmstadt, Germany
[2]Institute for Chemistry and Technology of Materials, Graz University of Technology, Stremayrgasse 9, 8010 Graz, Austria

[a)]Authors to whom correspondence should be addressed: zhao@ceramics.tu-darmstadt.de and jurij.koruza@tugraz.at

ABSTRACT

Deconvoluting the extrinsic and intrinsic contributions to electrostrain is of great importance to understand the hardening mechanism of piezoceramics. Here, *in situ* electric-field high-energy x-ray diffraction measurements are performed to investigate the polycrystalline barium calcium titanate hardened by precipitation, a recently developed hardening technique that pins domain walls with fine intragranular precipitates. The effect of precipitates on extrinsic and intrinsic mechanisms is examined. Under a low-frequency and large-signal field, the precipitates suppress non-180° wall motion, which is the major source of loss, by 40%. Anisotropy is observed in the field-induced lattice strain, which is dominantly contributed by an intergranular effect instead of pure piezoelectricity. At small fields, the lattice strain is barely affected by precipitates, while both lattice strain and strain from non-180° domain wall motion are suppressed and are coupled with each other at large fields, leading to an unchanged relative percentage of the extrinsic contribution.

The electrostrain of a ferroelectric material during the application of an electric field is contributed by intrinsic and extrinsic mechanisms.[1–3] The intrinsic contribution refers to the strain from lattice response, e.g., polarization extension/contraction and polarization rotation, while the extrinsic contribution refers to the response of domain walls or interphase boundaries, e.g., domain wall motion and field-induced phase transition.[4,5] These two types of contributions are difficult to separate by macroscopic measurement. However, with the development of synchrotron radiation facilities, deconvoluting the intrinsic and extrinsic contributions by *in situ* electric-field x-ray diffraction (XRD) became possible and has been extensively utilized in various ferroelectric materials at different conditions.[6–10]

Understanding the extrinsic contribution to electrostrain is important for designing piezoelectrics for high-power applications. In these applications, the piezoelectrics are driven at resonance frequency and a large vibration velocity,[11] where the mechanical quality factor Q_m (i.e., the reciprocal of the mechanical loss tan θ) is the main parameter defining the figure of merit. Domain wall motion is the dominant origin of mechanical loss during vibration, which causes severe temperature rise.[10,12] In addition, the vibration amplitude of a

piezoelectric driven at resonance frequency is proportional to Q_m.[13] To reduce mechanical loss and enhance Q_m, hardening is adopted to suppress domain wall motion.[13,14] The state-of-the-art piezoelectric hardening is done by chemical doping, which introduces charged point defects, usually oxygen vacancies, to establish an internal bias field and to stabilize the ferroelectric domains.[15–18] However, the mobility of oxygen vacancies leads to a deterioration of the hardening effect at high vibration velocities, increased temperature, or even with time.[19,20]

Alternative hardening methods are based on the composite approach in which secondary-phase particles are introduced to stabilize domains.[21,22] The hardening mechanism was considered to originate from the strain incompatibility between piezoelectric matrix and secondary-phase particles.[21] However, the introduction of secondary-phase particles into the powder mixture before the sintering step renders them embedded into the grain boundaries and triple junctions. This leads to locally limited influence on the domain walls in the grain interior. Recently, precipitation hardening was proposed for ferroelectric ceramics, which enables to introduce fine secondary-phase precipitates into the grain interior, acting as pinning centers for domain wall

motion.[23,24] The advantage of hardening using a secondary phase is that the hardening effect can be stable at large vibration velocities,[25] at high temperatures,[26] and with time, since the secondary-phase particles are more stable than oxygen vacancies.

In a model system $Ba_{0.7}Ca_{0.3}TiO_3$ (BCT), the samples with precipitates have an enhanced mechanical quality factor Q_m, decreased unipolar strain-field hysteresis, and suppressed large-signal polarization.[23] All these changes in property hint at a hardening effect. Transmission electron microscopy (TEM) has revealed a refinement of the domains in the vicinal region, which could be the origin of domain wall pinning. However, a bridge between the precipitate effect on the static domain structure and macroscopic property changes is missing, i.e., there is no experimental observation of the precipitate effect on the dynamic domain response to electric field. With *in situ* electric-field XRD, it is possible to extract the extrinsic contribution from the non-180° domain wall motion, and therefore quantify the effect of precipitates on it.

In the present work, *in situ* electric-field XRD was performed to deconvolute the extrinsic and intrinsic contributions in BCT samples without and with precipitates. The effect of precipitates on the dynamic response to the electric field was monitored by comparing the non-180° domain wall motion and field-induced lattice strain in the two samples. The relationship between the intrinsic and extrinsic contributions to electrostrain, as well as the relative extrinsic contribution, is discussed. This work provides a direct observation of the effect of precipitates on the non-180° domain wall motion and field-induced lattice strain under low-frequency, large-signal electric fields, enabling a better understanding of precipitation hardening.

The polycrystalline BCT samples were synthesized by the solid-state reaction method. The starting powders were $BaCO_3$ (Alfa Aesar, 99.95%), $CaCO_3$ (Alfa Aesar, 99.99%), and TiO_2 (Alfa Aesar, anatase, 99.6%). The detailed process was reported elsewhere.[23] The as-synthesized, sintered, and quenched samples are single phase without precipitates. To introduce the precipitates, the aging process was conducted by annealing the quenched samples at 1200 °C for 72 h and then at 1300 °C for 24 h. The samples were cut into dimension of $5 \times 1.5 \times 1\ mm^3$, and the two opposite $5 \times 1.5\ mm^2$ faces were electroded with Ag paste for the *in situ* electric-field XRD measurement.

In situ electric-field XRD was conducted at the beamline P02.1 at the Deutsche Elektronen-Synchrotron (DESY). The energy of the x rays was 60 keV (wavelength: 0.2073 Å). A schematic of the experimental setup is depicted in Fig. 1(a). Transmission geometry was adopted in combination with a two-dimensional detector; the sample-to-detector distance was set as ~120 cm. A customized sample stage designed for *in situ* electric-field XRD measurement is depicted in the inset of Fig. 1(a). The sample was immersed into the silicone oil, and its bottom electrode was in contact with the metal base, which was connected to high voltage. The top electrode was connected to the ground through a metal wire.

Before the *in situ* electric-field XRD measurement, the samples were poled at 4 kV/mm for 15 min at room temperature. The d_{33} values of the as-poled samples are 88 pC/N (without precipitates) and 86 pC/N (with precipitates). During the diffraction measurement, an electric field with a unipolar triangular waveform was applied, and the applied field direction was the same as that of the poling field. The field was ramped up from 0 to 3 kV/mm in 25 s and ramped down to
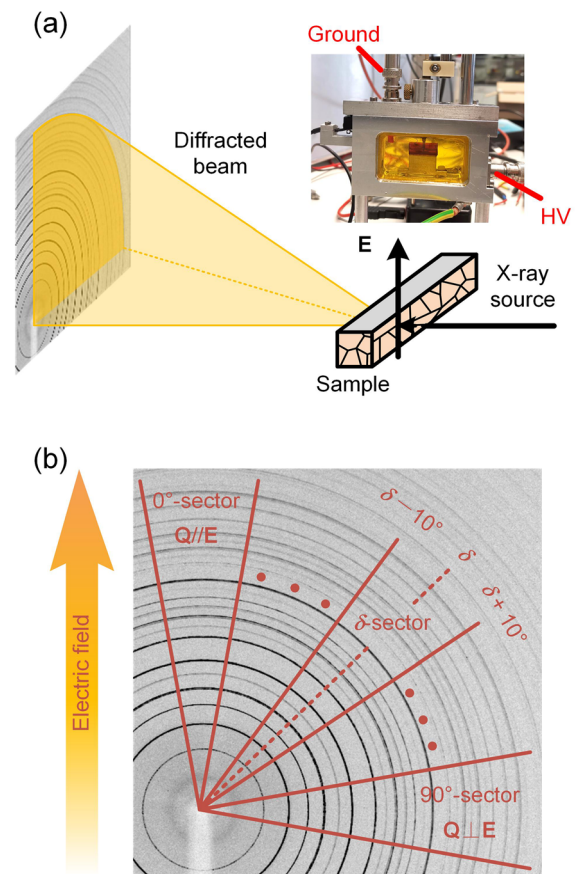

FIG. 1. (a) Experimental setup for the *in situ* electric-field XRD measurement. A photo of the sample stage is depicted in the inset. (b) Sector division for the two-dimensional pattern.

0 kV/mm at the same rate. XRD patterns were collected continuously during the application of field, with an exposure time of 0.5 s for each pattern.

The obtained 2D patterns were divided into 10 sectors to study the orientation-dependent structural response, as depicted in Fig. 1(b). Each sector has an angular range of 20°, which is slightly larger than the range commonly adopted, in order to have better statistics since the grain size of the samples is large (~15 μm). The directional difference δ between the scattering vector **Q** of each sector and the applied field **E** is denoted by δ (the corresponding sector is denoted by δ-sector).

The crystallographic structure of the matrix BT_{ss} phase ($BaTiO_3$-rich BCT solid solution) at the virgin state was determined to be tetragonal (Rietveld refinement in Fig. S1, Tables S1 and S2). Unlike in some other materials,[27–29] no field-induced phase transition has been observed in the samples investigated in the present study. The quantification of non-180° domain wall motion was performed based on the intensity interchange of 002 and 200 reflections with field. An intensity interchange can be observed in both BCT samples without and with precipitates [Figs. 2(a) and 2(b)], namely, the 002 reflection increases and the 200 reflection decreases with increasing field. An opposite
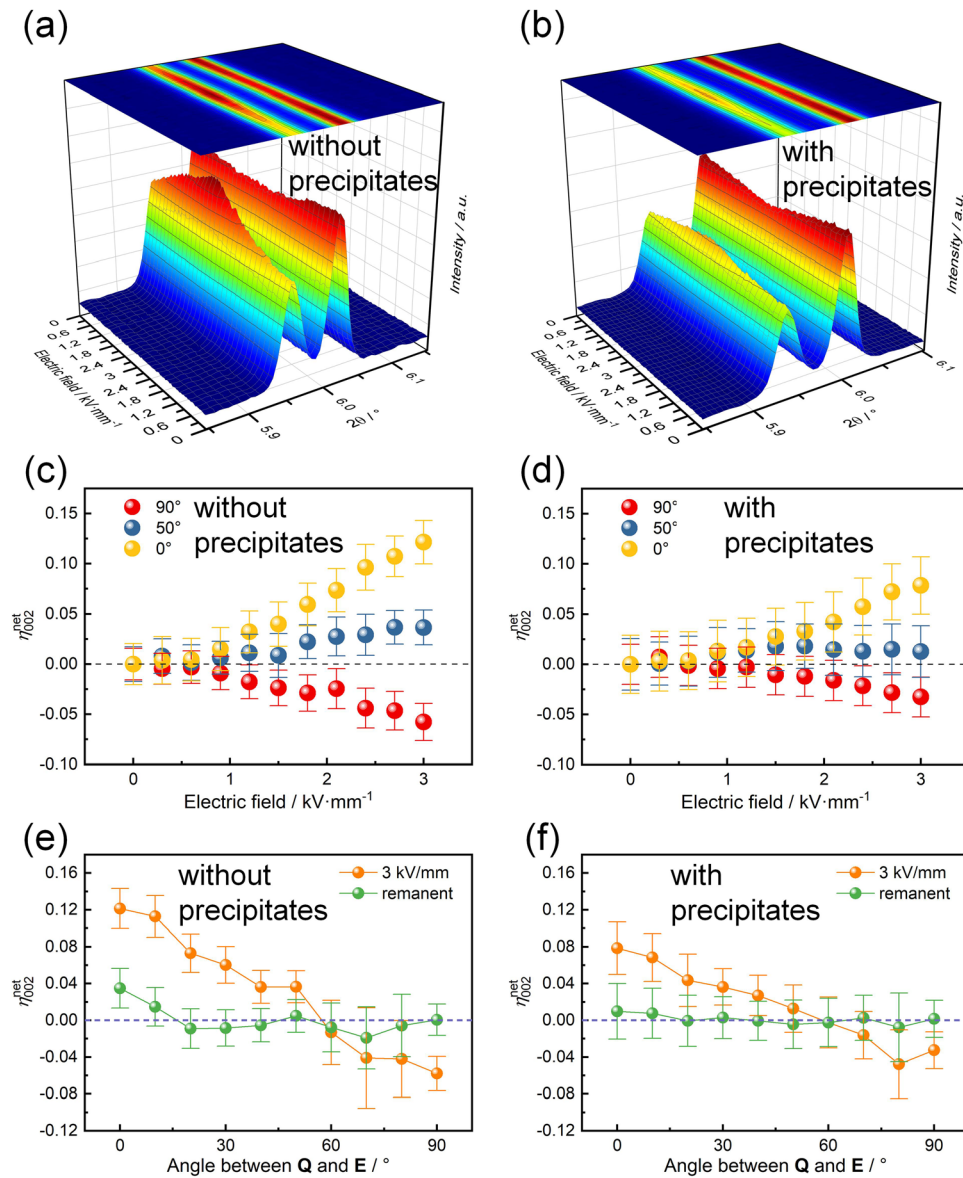
FIG. 2. Evolution of the 200 and 002 reflections of the BT_{ss} phase in samples (a) without and (b) with precipitates as a function of electric field. (c) and (d) η_{002}^{net} of samples with increasing field in directions with $0°$, $50°$, and $90°$ to the electric field. (e) and (f) η_{002}^{net} at the maximum field and remanent state as a function of the angle between $\mathbf{Q}$ and $\mathbf{E}$.

trend is observed for the two reflections as the electric field decreases. The extent of the non-180° domain wall motion is quantified by[8]

$$\eta_{002} = \frac{f_{002}}{3} - \frac{1}{3} = \frac{\dfrac{I_{002}}{I'_{002}}}{\dfrac{I_{002}}{I'_{002}} + 2 \times \dfrac{I_{200}}{I'_{200}}} - \frac{1}{3},$$ (1)

where f_{002} is the multiple of the 002-oriented domain fraction (*hkl*-oriented denotes the domains oriented with their *hkl* pole parallel to the $\mathbf{Q}$) with respect to that at the unpoled state. η_{002} represents the fraction of switched domains from 200- to 002-oriented compared to

the unpoled state. I_{hkl} and I'_{hkl} are the integrated intensities of the *hkl* reflections under electric field and at unpoled state, respectively, which were obtained by fitting of the 002 and 200 reflections with pseudo-Voigt shape function (representative fittings are depicted in Fig. S2), using the software LIPRAS.[30] Since the samples were poled, η_{002} is a non-zero value before the application of field. Therefore, η_{002}^{net} was derived by subtracting η_{002}^{pol}, which is the value of the state after the poling and before the *in situ* electric-field XRD measurement, to extract the fraction of switched domains induced only during application of the unipolar electric field. The absolute η_{002} values as a function of electric field are depicted in Fig. S3, where it can be noticed that the η_{002}^{pol} of the sample without precipitates is two times higher as that of

the sample with precipitates, indicating that precipitates also suppress the domain wall motion during the poling process.

The η_{002}^{net} of the samples without and with precipitates obtained from different δ-sectors as a function of electric field is depicted in Figs. 2(c) and 2(d). The different field dependences of η_{002}^{net} in the 0°-, 50°-, and 90°-sectors reflect an orientation-dependence of domain texture induced by the field. The η_{002}^{net} values of the sample with precipitates are smaller than those of the sample without precipitates in each sector, indicating that the non-180° domain wall motion is suppressed by precipitates. For both samples, the η_{002}^{net} exhibits negligible change below the electric field of ~0.6 kV/mm, which approximately coincides with the coercive field [0.65 and 0.75 kV/mm for samples without and with precipitates, respectively, Fig. S4(a)]. Thereafter, η_{002}^{net} changes almost linearly with field. This indicates that, for a poled sample, a critical field amplitude is required to activate substantial non-180° domain wall motion, and this critical field in comparable to the coercive field.

To study the orientation-dependence of non-180° domain wall motion, the η_{002}^{net} values at 3 kV/mm and at the remanent state (i.e., the state after the application of unipolar electric field) are plotted as a function of δ. For both samples, η_{002}^{net} is almost zero in the 60°-sector, indicating that the domain texture is least affected in the domains with their [001] direction 60° from the field. At the field of 3 kV/mm, the η_{002}^{net} values of the sample with precipitates are ~60% of that of the sample without precipitates in the sectors with δ of 0°–40° and 90° (the η_{002}^{net} values in the 50°–80° sectors are rather small and, thus, the η_{002}^{net} ratio between the samples with and without precipitates has a large error), indicating that the suppression of the non-180° domain wall motion from precipitates is nearly isotropic. The η_{002}^{net} values at the remanent state are close to zero in most sectors for both samples, indicating that the non-180°domain wall motion induced by the unipolar field is predominantly reversible. Considering that the samples were poled several days before the measurement, a natural aging leading to a reduction in macroscopic polarization by slow domain wall motion is possible, which was previously reported in BaTiO₃.[31] The natural aging can also be indicated by a slight drop in the d_{33} of the sample

without precipitates two days after the poling (from 88 to 86 pC/N), while the d_{33} remained unchanged for the sample with precipitates. The relatively large remanent η_{002}^{net} in the 0°- and 10°-sector of the sample without precipitates could be attributed to this depolarization process.

The longitudinal field-induced lattice strains with increasing field in $\langle 111\rangle$-, $\langle 002\rangle$-, and $\langle 022\rangle$-oriented cells are depicted in Figs. 3(a) and 3(b), which were derived by calculating the relative change of the d-spacing of different reflections in the 0°-sector. The strain analyzed with hkl reflections corresponds to the cells oriented with their $\langle hkl\rangle$ parallel to the field. Anisotropy is observed in field-induced lattice strain, and even negative field-induced lattice strain appears in some orientations. In general, the sample with precipitates has smaller field-induced lattice strain in all orientations when compared to the sample without precipitates.

The anisotropy of the field-induced strain is quantified by strain values in differently oriented cells at 3 kV/mm, presented in a polar plot. The angular coordinates represent the angle between the field and the [001] direction (polar axis of a tetragonal sample). The radial coordinates represent the amplitude of the field-induced lattice strain. Obviously, both samples feature anisotropy in the field-induced lattice strain. The largest positive field-induced lattice strain is found along a nonpolar axis for both samples. Negative strain is apparent in directions nearly parallel or perpendicular to the polar axis. Moreover, there are also some differences in the anisotropy of the samples without and with precipitates. For example, the maximum strain is found in the $\langle 111\rangle$ directions for the sample without precipitates and in the $\langle 121\rangle$ directions for the sample with precipitates; after aging, the lattice strain has a more significant decrease (more than 50%) in the $\langle 112\rangle$- and $\langle 111\rangle$-oriented cells than in other investigated orientations.

Anisotropy in field-induced lattice strain is usually attributed to polarization rotation[32] or intragranular effects.[9] Polarization rotation is an intrinsic feature of materials, which exhibit larger transversal dielectric susceptibility than the longitudinal one.[33] As a result, the maximum piezoelectric response is observed away from the polar axis, indicating that the polarization vector is easier to rotate than to
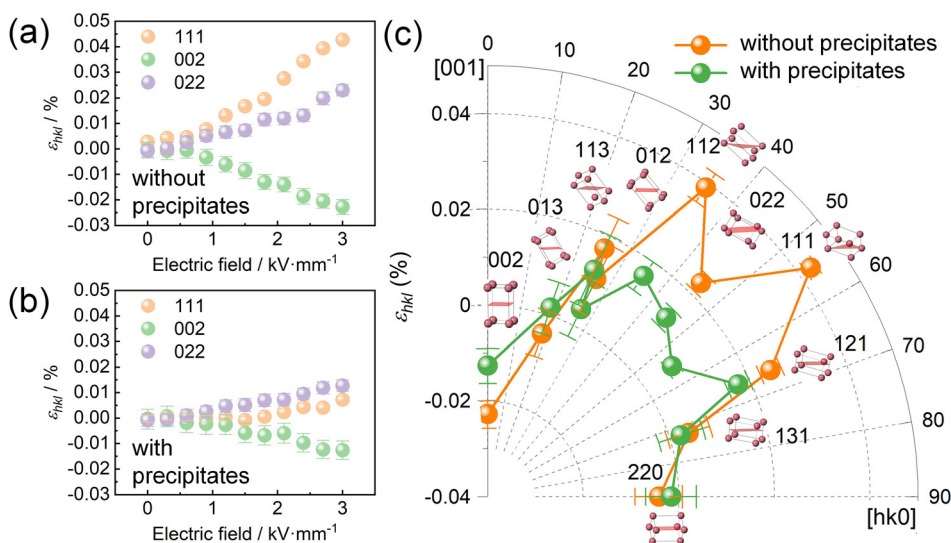
FIG. 3. (a) and (b) Longitudinal field-induced lattice strain in differently oriented cells. (c) Orientation dependence of the field-induced lattice strain regarding the angle between the electric field and the polar axis.

extend.[34] The intergranular effect refers to the elastic deformation of grains, which is due to the difference in non-180° domain wall motion of differently oriented grains and an adaptation of compatibility strains in a polycrystalline material. The intergranular effect has been previously reported in polycrystalline $Pb(Zr,Ti)O_3$, $(Na_{1/2}Bi_{1/2})TiO_3$-$BaTiO_3$, and $BiFeO_3$ materials.[35–38]

For the BCT samples, the negative field-induced lattice strain in the [001]-oriented cells is attributed to the intergranular effect, where non-180° domain wall motion is most favored and is, thus, subjected to compressive stress from surrounding grains. Such negative lattice strain has also been observed in $(Ba,Ca)(Zr,Ti)O_3$ polycrystalline materials.[39] In addition, an inflection point can be noticed in the field-induced lattice strain of the sample without precipitates at the field of ~0.6 kV/mm [Fig. 3(a)], above which the lattice strain increases stronger with field. For a freestanding crystal without intergranular effect, a continuous increase in lattice strain proportional to the field amplitude is expected. This inflection feature coincides with the change of η_{002}^{net} with field, indicating that above 0.6 kV/mm, there is a large fraction of field-induced lattice strain strongly coupled with non-180° domain wall motion in the sample without precipitates, which is due to the intergranular effect. For the sample with precipitates, since the non-180° domain wall motion is largely suppressed, the part of lattice strain coupled with domain wall motion is also reduced. Therefore, the samples with precipitates are featured with smaller negative lattice strain,

weaker anisotropy [Fig. 3(c)], and an insignificant inflection point in the lattice strain-field curve [Fig. 3(b)].

Another interesting observation is that the lattice strain in ⟨111⟩- and ⟨112⟩-oriented cells is significantly reduced after the introduction of precipitates, compared to other orientations. Considering the intergranular effect discussed above, the cells with these two orientations are most affected, since they have minimum strain from non-180° domain wall motions and are subjected to the largest tensile elastic strain from the material.[7] As the sample with precipitates exhibits suppressed non-180° domain wall motions, the elastic compatibility strains also reduce, which is most significant in the ⟨111⟩- and ⟨112⟩-oriented cells.

The macroscopic electrostrain contributed by lattice strain and non-180° domain wall motion are calculated by Eqs. (2) and (3), respectively,[4,40]

$$S_{zz,lat} = \frac{\sum_{hkl} f_{hkl}(0°)m_{hkl}\varepsilon_{hkl}}{\sum_{hkl} f_{hkl}(0°)m_{hkl}}, \quad (2)$$

$$S_{zz,DW} = S_{spon}(\delta) \times \int_0^{\frac{\pi}{2}} [f_{hkl}(\delta,E) - 1]\cos^2\delta\sin\delta\,d\delta, \quad (3)$$

where $S_{zz,lat}$ and $S_{zz,DW}$ represent the longitudinal strain contributed by lattice strain and non-180° domain wall motion, respectively. f_{hkl} is
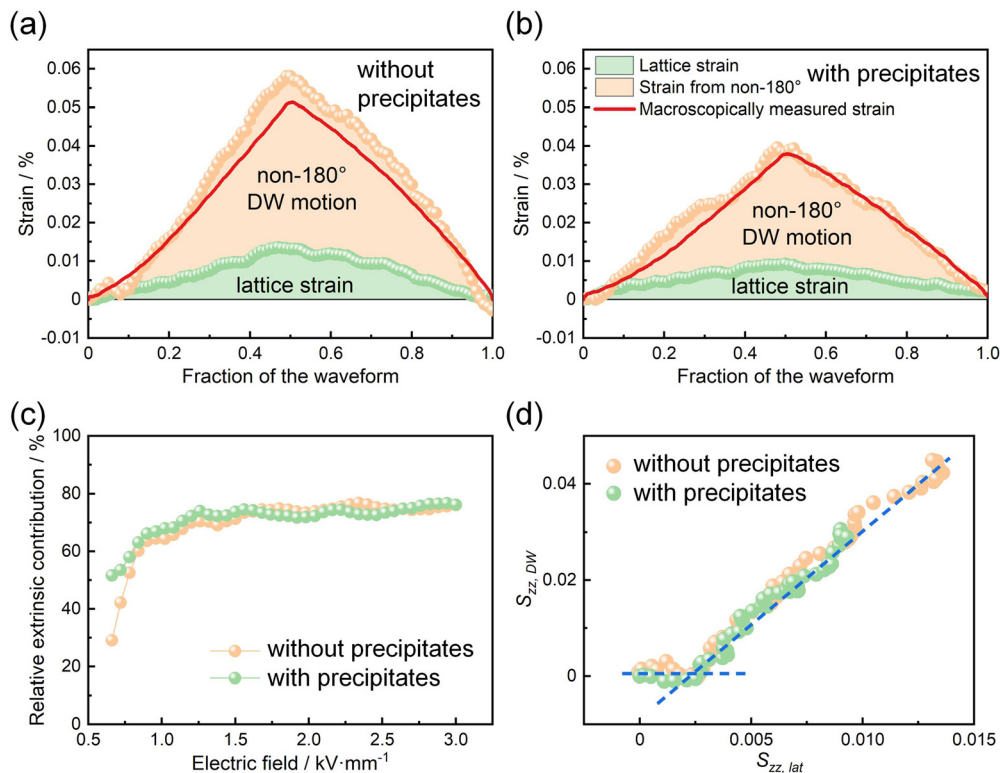
FIG. 4. (a) and (b) Intrinsic and extrinsic contributions to the macroscopic strain calculated based on diffraction data. The macroscopically measured unipolar strain is indicated by the red solid line. (c) Relative extrinsic contribution to the macroscopic strain during the application of electric field. (d) Relationship between the extrinsic strain and intrinsic strain in the samples without and with precipitates during the field increasing process.

the texture parameter of hkl-oriented domains, which were obtained in a similar manner as the calculation of f_{002}. m_{hkl} is the multiplicity of the hkl reflection and determined by crystallographic symmetry. S_{spon} is the ferroelastic spontaneous lattice strain, which is expressed by the lattice parameter ratio c/a-1 for tetragonal sample. Reflections of 111, {200}, {210}, {211}, {220}, {310}, and {311} were adopted for the calculation of $S_{zz,lat}$.

The $S_{zz,lat}$ and $S_{zz,DW}$ of the BCT samples without and with precipitates are depicted in Figs. 4(a) and 4(b), respectively, as a function of fraction of the applied field waveform. The orange area and green area represent the $S_{zz,DW}$ and $S_{zz,lat}$, respectively. The macroscopically obtained strain (optical displacement sensor) is indicated by the red solid lines, which is in a good agreement with the sum of $S_{zz,DW}$ and $S_{zz,lat}$. The total strain of the sample with precipitates is smaller than that of the sample without precipitates. From the areas under the intrinsic and extrinsic strain in Figs. 4(a) and 4(b), it can be estimated that the $S_{zz,DW}$ is larger than the $S_{zz,lat}$ for both samples.[41]

The relative extrinsic contribution (i.e., the ratio between the $S_{zz,DW}$ and calculated total strain) during increasing field is depicted in Fig. 4(c). The result below the field of 0.6 kV/mm is not provided since the strain values are too small (at or below 0.0001%). Therefore, the ratio is extremely scattered and not reliable. The relative extrinsic contribution increases with increasing field and stabilizes at ∼75% above the field of ∼1.25 kV/mm for both samples. This indicates that the precipitates lead to a decrease in the $S_{zz,DW}$ and $S_{zz,lat}$ by a similar percentage at large and low-frequency field.

As discussed above, the lattice strain consists of a piezoelectric part (polarization extension or rotation) and an elastic part (intergranular effect). A question arises whether the decreased $S_{zz,lat}$ in the sample with precipitates is due to a direct suppression of intrinsic piezoelectric response or is a consequence of a suppression of non-180° domain wall motion, so that the coupled lattice strain decreases. The relationship between the $S_{zz,DW}$ and $S_{zz,lat}$ with increasing field is depicted in Fig. 4(d). Two regimes can be observed, which are separated by the inflection point. In the first regime, only $S_{zz,lat}$ increases, while $S_{zz,DW}$ remains almost unchanged. In the second regime, both $S_{zz,DW}$ and $S_{zz,lat}$ increase and have a linear relationship, indicating a strong coupling between them. It can be suggested that the intrinsic piezoelectric response dominates the $S_{zz,lat}$ when the field is small since non-180° domain wall motion is barely activated, while the intergranular effect becomes prominent when at large field. This can be further evidenced by the relationship between $S_{zz,lat}$ and field (Fig. S5), where both samples share a same strain-field slope below the field of ∼0.75 kV/mm, and the slope diverges above this field.

In summary, the effect of precipitates on the lattice strain and the strain from non-180° domain wall motion of BCT samples has been investigated by *in situ* electric-field high-energy XRD. The precipitates reduced the extent of non-180° domain wall motion under large field by 40%. An anisotropy is observed in field-induced lattice strain, which is predominantly attributed to intergranular strain compatibility, and this anisotropy is reduced in the sample with precipitates. The precipitates have negligible influence on the lattice strain of BCT under a small field, while a prominent effect on the lattice strain from precipitates is observed through the intergranular effect under a large field.

See the supplementary material for the complete results of the Rietveld refinement, macroscopically measured polarization-field and strain-field hysteresis loops, and the intrinsic strain as a function of the electric field.

AUTHOR DECLARATIONS
Conflict of Interest

The authors have no conflicts to disclose.

Author Contributions

Changhao Zhao: Conceptualization (equal); Data curation (equal); Formal analysis (equal); Investigation (equal); Methodology (equal); Visualization (equal); Writing – original draft (equal); Writing – review & editing (equal). **Mao-Hua Zhang:** Data curation (equal); Formal analysis (equal); Investigation (equal); Writing – review & editing (equal). **Jürgen Rödel:** Funding acquisition (equal); Project administration (lead); Writing – review & editing (equal). **Jurij Koruza:** Data curation (equal); Funding acquisition (equal); Writing – review & editing (equal).

DATA AVAILABILITY

The data that support the findings of this study are available from the corresponding authors upon reasonable request.

REFERENCES

[1]Q. M. Zhang, H. Wang, N. Kim, and L. E. Cross, J. Appl. Phys. **75**, 454 (1994).
[2]D. J. Kim, J. P. Maria, A. I. Kingon, and S. K. Streiffer, J. Appl. Phys. **93**, 5568 (2003).
[3]D. Damjanovic and M. Demartin, J. Phys. D: Appl. Phys. **29**, 2057 (1996).
[4]J. L. Jones, M. Hoffman, J. E. Daniels, and A. J. Studer, Appl. Phys. Lett. **89**, 092901 (2006).
[5]M. Zhang, C. Zhao, L. Fulanović, J. Rödel, N. Novak, A. Schökel, and J. Koruza, Appl. Phys. Lett. **118**, 132903 (2021).
[6]G. Tutuncu, J. S. Forrester, J. Chen, and J. L. Jones, Acta Mater. **137**, 45 (2017).
[7]A. Pramanick, D. Damjanovic, J. E. Daniels, J. C. Nino, and J. L. Jones, J. Am. Ceram. Soc. **94**, 293 (2011).
[8]J. L. Jones, E. B. Slamovich, and K. J. Bowman, J. Appl. Phys. **97**, 34113 (2005).
[9]D. A. Hall, A. Steuwer, B. Cherdhirunkorn, T. Mori, and P. J. Withers, J. Appl. Phys. **96**, 4245 (2004).
[10]M. Slabki, L. K. Venkataraman, S. Checchia, L. Fulanović, J. Daniels, and J. Koruza, Phys. Rev. B **103**, 174113 (2021).
[11]K. Uchino, "Chapter 17—High-power piezoelectrics and loss mechanisms," in *Advanced Piezoelectric Materials*, 2nd ed. (Woodhead Publishing, 2017).
[12]K. H. Härdtl, Ceram. Int. **8**, 121 (1982).
[13]K. Uchino, *Ferroelectric Devices* (CRC Press of Taylor & Francis Group, Boca Raton, 2010).
[14]T. N. Nguyen, H. C. Thong, Z. X. Zhu, J. K. Nie, Y. X. Liu, Z. Xu, P. S. Soon, W. Gong, and K. Wang, J. Mater. Res. **36**, 996 (2021).
[15]S. Takahashi, Jpn. J. Appl. Phys. **20**, 95 (1981).
[16]G. H. Jonker, J. Am. Ceram. Soc. **55**, 57 (1972).
[17]X. Ren, Nat. Mater **3**, 91 (2004).

[18] Y. A. Genenko, J. Glaum, M. J. Hoffmann, and K. Albe, Mater. Sci. Eng. B **192**, 52 (2015).

[19] S. Takahashi and S. Hirose, Jpn. J. Appl. Phys. **32**, 2422 (1993).

[20] J. Glaum, Y. A. Genenko, H. Kungl, L. Ana Schmitt, and T. Granzow, J. Appl. Phys. **112**, 34103 (2012).

[21] Lalitha K. V., L. M. Riemer, J. Koruza, and J. Rödel, Appl. Phys. Lett. **111**, 022905 (2017).

[22] Lalitha K. V., J. Koruza, and J. Rödel, Scr. Mater. **169**, 92 (2019).

[23] C. Zhao, S. Gao, T. Yang, M. Scherer, J. Schultheiß, D. Meier, X. Tan, H. J. Kleebe, L. Q. Chen, J. Koruza, and J. Rödel, Adv. Mater. **33**, 2102421 (2021).

[24] C. Zhao, S. Gao, H. Kleebe, X. Tan, J. Koruza, and J. Rödel, Adv. Mater. **34**, 2202379 (2022).

[25] M. Slabki, K. V. Lalitha, J. Rödel, and J. Koruza, Acta Mater. **227**, 117703 (2022).

[26] M. Slabki, L. K. Venkataraman, T. Rojac, J. Rödel, and J. Koruza, J. Appl. Phys. **130**, 14101 (2021).

[27] M. Zhang, C. Shen, C. Zhao, M. Dai, F. Yao, B. Wu, J. Ma, H. Nan, D. Wang, Q. Yuan, L. L. Da Silva, L. Fulanović, A. Schökel, P. Liu, H. Zhang, J. Li, N. Zhang, K. Wang, J. Rödel, and M. Hinterstein, Nat. Commun. **13**, 3434 (2022).

[28] M. Hinterstein, J. Rouquette, J. Haines, P. Papet, M. Knapp, J. Glaum, and H. Fuess, Phys. Rev. Lett. **107**, 77602 (2011).

[29] J. E. Daniels, W. Jo, J. Rödel, V. Honkimaeki, and J. L. Jones, Acta Mater. **58**, 2103 (2010).

[30] G. Esteves, K. Ramos, C. M. Fancher, and J. L. Jones (2017). "LIPRAS: Line-profile analysis software," MathWorks. https://doi.org/10.13140/RG.2.2.29970.25282/3.

[31] W. P. Mason, J. Acoust. Soc. Am. **27**, 73 (1955).

[32] E. H. Kisi, R. O. Piltz, J. S. Forrester, and C. J. Howard, J. Phys.: Condens. Matter **15**, 3631 (2003).

[33] D. Damjanovic, IEEE Trans. Ultrason. Ferroelectr. Freq. Control **56**, 1574 (2009).

[34] M. Davis, M. Budimir, D. Damjanovic, and N. Setter, J. Appl. Phys. **101**, 54112 (2007).

[35] J. L. Jones, A. Pramanick, J. C. Nino, S. Maziar Motahari, E. St Ndag, M. R. Daymond, and E. C. Oliver, Appl. Phys. Lett. **90**, 172909 (2007).

[36] N. H. Khansur, T. Rojac, D. Damjanovic, C. Reinhard, K. G. Webber, J. A. Kimpton, and J. E. Daniels, J. Am. Ceram. Soc. **98**, 3884 (2015).

[37] C. Zhao, D. Hou, C. Chung, H. Zhou, A. Kynast, E. Hennig, W. Liu, S. Li, and J. L. Jones, Acta Mater. **158**, 369 (2018).

[38] M. J. Hossain, Z. Wang, N. H. Khansur, J. A. Kimpton, J. Oddershede, and J. E. Daniels, Appl. Phys. Lett. **109**, 092905 (2016).

[39] M. C. Ehmke, N. H. Khansur, J. E. Daniels, J. E. Blendell, and K. J. Bowman, Acta Mater. **66**, 340 (2014).

[40] M. R. Daymond, J. Appl. Phys. **96**, 4263 (2004).

[41] H. Kungl, R. Theissmann, M. Knapp, C. Baehtz, H. Fuess, S. Wagner, T. Fett, and M. J. Hoffmann, Acta Mater. **55**, 1849 (2007).